

Blackening of Pompeian Cinnabar Paintings: X-ray Microspectroscopy Analysis

Marine Cotte,^{*,†} Jean Susini,[†] Nicole Metrich,[‡] Alessandra Moscato,[§] Corrado Gratzu,[§] Antonella Bertagnini,^{||} and Mario Pagano[⊥]

European Synchrotron Radiation Facility, BP 220, 38043 Grenoble Cedex, France, Laboratoire Pierre Süe, CEA-CNRS, CE-Saclay, 91191 Gif sur Yvette, France, Dipartimento di Scienze della Terra, Università di Pisa, Via S. Maria, 53. 56126 Pisa, Italy, Istituto Nazionale di Geofisica e Vulcanologia, Sezione di Pisa, Via della Faggiola, 32. 56126 Pisa, Italy, and Soprintendenza per i Beni Archeologici del Molise, Via Chiarinzia 14, 86100 Campobasso, Italy

Red Pompeian paintings, very famous for their deep intensity, are currently suffering from darkening. The origins of this darkening degradation are not clearly identified yet and remain a major issue for curators. In the specific case of cinnabar (HgS)-based red pigment, a photoinduced conversion into black metacinnabar is usually suspected. This work is focused on the blackening of red cinnabar paintings coated on a sparry calcite mortar. Different samples exhibiting different levels of degradation were selected upon visual observations and analyzed by synchrotron-based microanalytical techniques. Atomic and molecular compositions of the different debased regions revealed two possible degradation mechanisms. On one hand, micro X-ray fluorescence elemental maps show peculiar distributions of chlorine and sulfur. On the other hand, X-ray absorption spectroscopy performed at both Cl and S K-edges confirms the presence of characteristic degradation products: (i) Hg–Cl compounds (e.g., corderoite, calomel, and terlinguaite), which may result from the reaction with exogenous NaCl, in gray areas; (ii) gypsum, produced by the calcite sulfation, in black coatings. Metacinnabar is never detected. Finally, a cross section was analyzed to map the in-depth alteration gradient. Reduced and oxidized sulfur distributions reveal that the sulfated black coating consists of a ~5- μm -thick layer covering intact cinnabar.

Pigments color can sometimes evolve, unexpectedly, from the painter's or curator's point of view. The most common degradation of red mercury sulfide, used in a cinnabar natural form or in a vermilion synthetic form, is turning into black or silver-gray. This phenomenon is rather capricious and does not happen systematically. Since Antiquity, cinnabar was often used in paintings, even if it was known to suffer from sunlight and humidity degradation.^{1,2} However, the degradation process is far from being completely

understood. Furthermore, several mechanisms seem to be involved in this blackening, leading to different chemical species. Up to recent times, the most advanced hypothesis was the phase transformation of red hexagonal cinnabar into black cubic metacinnabar by action of light.^{3–5} Yet, chlorine was shown to be possibly involved in the darkening of natural cinnabar^{6,7} and in the formation of white and gray crusts in vermilion paintings.^{8,9}

Samples come from wall paintings of "Villa Sora", in Torre del Greco near Pompeii. The house was buried by pumice deposits of the 79 A.D. famous eruption of Vesuvius. They crossed centuries with a good resistance to degradation and they were still red when excavated. The excavation work started in 1988 and finished in 1992: unfortunately the cinnabar paint layers have exhibited increasing degradation since 1990, when the excavation was still in progress. The main expectation of curators was to determine the chemical nature of degradation products in order to adapt their treatments and to restrain further blackening. In particular, the possible presence of metacinnabar remained an underlying question. It was thus necessary to clearly identify the atomic and molecular compositions of the different debased areas. Such analytical studies require challenging experimental conditions:

- (i) A low detection limit is necessary to probe trace elements, which can act, even at low concentrations, as catalyst in degradation processes.
- (ii) A high chemical sensitivity is mandatory to identify the specific chemical signatures of molecular compounds involved in the different degradation processes.
- (iii) The degradation evolution must be considered as a tridimensional process, and therefore, a complete analysis requires both in-plane and in-depth information. Furthermore, the size of

* To whom correspondence should be addressed. E-mail: cotte@esrf.fr.
Phone: +33 4 76 88 21 27. Fax: +33 4 76 88 27 85.

[†] European Synchrotron Radiation Facility.

[‡] Laboratoire Pierre Süe, CEA-CNRS.

[§] Università di Pisa.

^{||} Istituto Nazionale di Geofisica e Vulcanologia.

[⊥] Soprintendenza per i Beni Archeologici del Molise.

(1) Plinio Caio Seniore, *Naturalis Historia*, lib. XXXIII, 113 and passim.

(2) Aurisicchio, C.; Ferro, D.; Martinelli, G.; Cesaro, S. N.; Rapinesi, I. A. J. *Cultural Heritage* **2002**, 3, 107–116.

(3) Gettens, R. J.; Feller, R. L.; Chase, W. T. *Stud. Conserv.* **1972**, 17, 45–69.

(4) Liberti, S. *Bollettino dell'Istituto Centrale del Restauro* **1950**, 3–4, 45–64.

(5) Zafirooulos, V.; Balas, C.; Manousaki, A.; Marakis, Y.; Maravelaki-Kalaitzaki, P.; Melesanaki, K.; Pouli, P.; Stratoudaki, T.; Klein, S.; Hildenhagen, J.; Dickmann, K.; Luk'Yanchuk, B. S.; Mujat, C.; Dogariu, A. J. *Cultural Heritage* **2003**, 4, 249s–256s.

(6) McCormack, J. K.; Dickson, F. W.; MP Leshendok, M. P. *Am. Mineral.* **1991**, 76, 1715–1721.

(7) McCormack, J. K. *Miner. Deposita* **2000**, 35, 796–798.

(8) Spring, M.; Grout, R. *Natl. Gallery Technol. Bull.* **2002**, 23, 50–61.

(9) Keune, K.; Boon, J. J. *Anal. Chem.* **2005**, 77, 4742–4750.

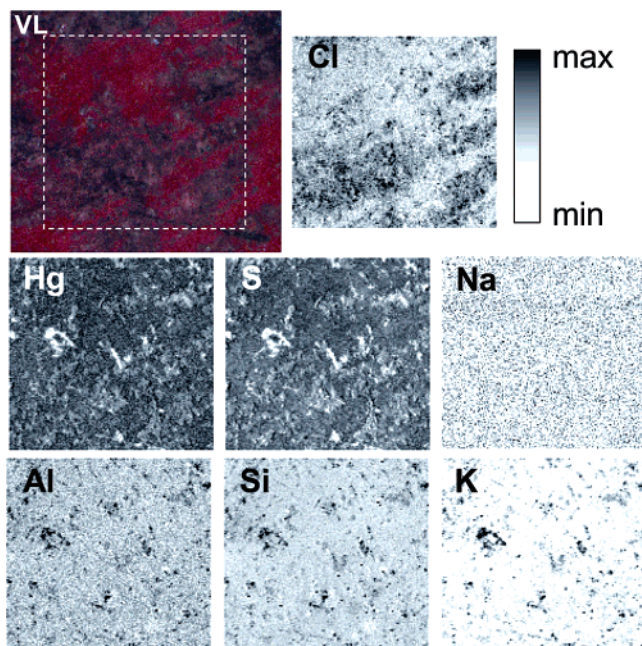


Figure 1. Visible light microscopy image (VL) and atomic distribution (Cl, Hg, S, Na, Al, Si, K) of S2 (obtained by μ -XRF with an exciting beam of 3.9 keV). Pixel size, $50 \times 50 \mu\text{m}^2$; map size, $7 \times 7 \text{ mm}^2$; dwell time, 0.3 s.

heterogeneities suggests use of microprobe techniques with a submicrometer resolution.

The ID21 X-ray microscopy beam line of the ESRF provides a well-suited instrument that fulfills the above-mentioned requirements. The combination of micro X-ray fluorescence (μ -XRF) mapping and of micro X-ray absorption spectroscopy (μ -XANES) at chlorine and sulfur K-edges allowed a systematic screening of four samples originated from Villa Sora in Torre del Greco, Italy.

This work aimed at identifying the degradation reactions and the relationship between morphology, color, and chemical compositions. No evidence for transformation to metacinnabar was found. Conversely, various routes of degradation are proposed. They implicate at least two concomitant reactions: the formation of mercury chloride products and the sulfation of lime (pictorial mortar) into gypsum. The possible roles of exogenous compounds (NaCl, soil dust, ashes) and the color of degradation products are briefly addressed.

EXPERIMENTAL SECTION

(a) Samples. A set of four samples of cinnabar painting coming from a wall painting excavated in 1988 was collected to investigate the various degradation aspects. They correspond to different degradation states:

Sample 1 (S1). S1 does not show any observable signs of degradation. It presents a homogeneous flat red aspect.

Sample 2 (S2). S2 exhibits a moderate level of alteration (Figure 1VL). The red areas are flat and look rather intact. The altered regions appear as heterogeneous patchy stripes with two dominant colors: dark gray, or following Spring's terminology "lilac-gray color",⁸ and light gray. Furthermore, a visible thin black line crosses the bottom right corner of the image. Finally, pictures at higher magnifications and grazing illumination (not shown here) reveal other domains scattered on the surface: some rust-colored

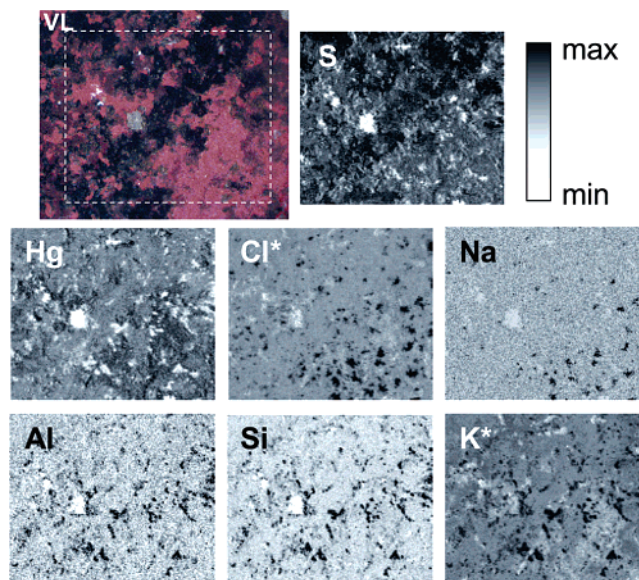


Figure 2. VL and atomic distribution (S, Hg, Cl, Na, Al, Si, K) of S3 (obtained by μ -XRF with an exciting beam of 3.9 keV). Pixel size, $50 \times 50 \mu\text{m}^2$; map size, $8 \times 7 \text{ mm}^2$; dwell time, 0.3 s. * Symbol designates the maps plotted in log scale.

protrusions, which consist of white and orange particles, and some small black bulging spots. It is worth noting that similarities exist with the description of vermilion blackening made by Spring and Grout on various egg tempera and oil paintings.⁸

Sample 3 (S3). The main degradation patterns in S3 are flat, compact, black coatings (Figure 2VL), with some brown-black shades that may indicate concentration gradients. They are generally darker, and less heterogeneous than gray degradations of S2. Contrary to S1 and S2, the red parts of S3 are in hollow and appear more friable, powdery, and whiter than intact cinnabar. They may result from abrasion of a previously degraded surface. Rust spots are also observed on S3, to a greater extent than on S2 (observations at higher magnifications and grazing illumination, not shown here). They are often found at the boundary of brown or black domains. As discussed later, chemical mapping will highlight the various observed domains on S2 and S3 (Figures 1 and 2).

Sample 4 (S4). A transversal cross section of an altered region was obtained by previous embedding of the specimen in polyester resin to completely preserve the pictorial layer during the grinding and polishing processes with sand papers and oily lubricant.

Reference Compounds. Quantitative X-ray absorption spectroscopy requires reference compounds for calibration. Most of them were purchased from Sigma, except mineral lapis lazuli, cinnabar (from Almadén), metacinnabar, corderoite, eglestonite, and terlinguaite, which came from museums collections.

(b) Instruments. X-ray fluorescence maps and X-ray absorption spectroscopy analyses were both performed at the X-ray microscopy beam line, ID21, at the ESRF (Grenoble, France) (www.esrf.fr/UsersAndScience/Experiments/Imaging/ID21).¹⁰ The scanning X-ray microscope has a tunable energy ranging from 2.1 to 7.2 keV and is optimized for very low background and low

(10) Susini, J.; Salomé, M.; Fayard, B.; Ortega, R.; Kaulich, B. *Surf. Rev. Lett.* **2002**, *9*, 203–211.

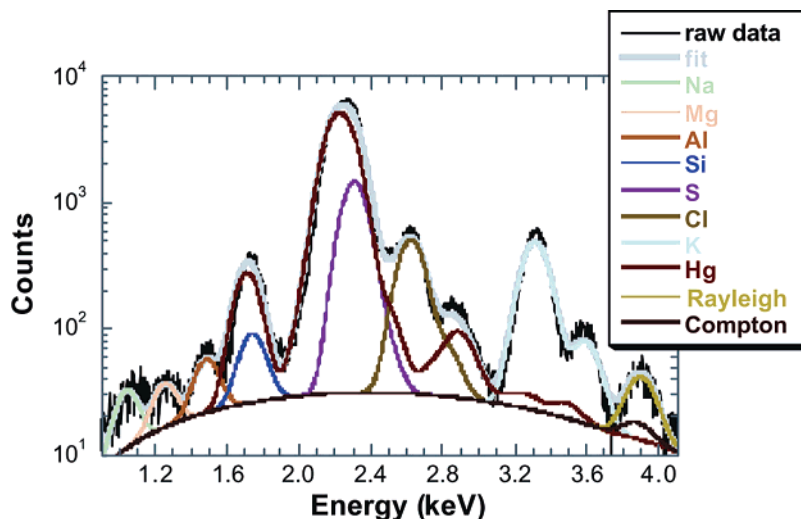


Figure 3. Example of μ -XRF spectrum, fitted with PyMca. Acquisition on S2 (light gray area), with a 50- μ m pinhole; dwell time, 300 s.

detection limits. The fluorescence excitation is stimulated with a highly monochromatic beam by means of a fixed-exit, double-crystal Si(111) monochromator, located upstream of the microscope, and which provides an energy resolution of $\Delta E/E = 10^{-4}$. The sample is mounted vertically on a high-precision piezoelectric stage and raster scanned horizontally and vertically, with respect to the X-ray microprobe, which remains fixed, to produce a two-dimensional image. Fresnel zone plates are used as focusing optics to generate a submicrometer X-ray probe by geometrical demagnification of the synchrotron source. The microfluorescence signal is collected in the horizontal plane perpendicular to the incident beam direction by using a small-area (30 mm²), HPGc solid-state, energy-dispersive detector, which is coupled to state-of-the-art digital pulse processing electronics. The energy resolution of this detection system is 130 eV at 6 keV. The detector is collimated and targets the fixed area illuminated by the microprobe. The detection solid angle is, therefore, constant. An Io detector is inserted just upstream of the sample to normalize the signal in case of flux variation in the incoming beam (a few percent over several hours). The detection limit for elements ranging from Fe to P is ~ 10 ppm. It is worth noting that the incident X-ray beam is highly linearly polarized ($\sim 99.5\%$) with an electric field vector in the horizontal plane to minimize the background signals originating from elastic and inelastic scattering measured by the detector located at 90°. The setup is equipped with an on-line visible light microscope that allows the operator to keep track of the position of the specimen during the scans. The instrument is operated under vacuum in order (i) to minimize the air absorption, which is significant for light-element fluorescence lines, (ii) to avoid scattering from air, and (iii) to prevent sample contamination.

Furthermore, the molecular environment of a given element can then be characterized by tuning the energy of the probing X-ray photons across the absorption edge of this element (2.472 and 2.822 keV for S and Cl, respectively). The spectral features observed close to the absorption edge—referred to as X-ray absorption near edge structure (XANES)—reflect the molecular environment of a given absorbing atom and provide the basic mechanism for imaging with chemical sensitivity. The XANES calibration with standards (pure or well-identified compounds)

provides reference spectra for comparison. It is worth mentioning that the energy resolution of the energy-dispersive detector is good enough to prevent interference between S and Hg fluorescence signals originating from the most intense K-line of S and M-lines of Hg at 2.308 and 2.195 keV, respectively.

RESULTS

(a) Micro X-ray Fluorescence Analyses. To assess the correlation between atomic compositions and degradation signs, elemental maps of the surface (averaged probed depth of $\sim 5 \mu\text{m}$) of the three samples, S1, S2, and S3, were performed by use of the XRF microprobe. Characteristic areas of $\sim 0.5 \text{ cm}^2$ were selected and mapped with a pixel size of $50 \times 50 \mu\text{m}^2$ and an excitation energy of 3.9 keV. As shown in Figure 3, spectra analysis is difficult due to significant overlap of the fluorescence lines of atoms of interest. In particular Si, Hg, S, and Cl do interfere. The line deconvolution was performed by using dedicated software, PyMca. This program implements a Levenberg–Marquardt algorithm to fit the spectra with constraints on the fitting parameters (detector characteristics, detection geometry, matrix composition, exciting energy, etc.). A complete emission line series (i.e., M or L series) is fitted by taking into account theoretical intensity ratios and line emission energies. A more detailed description of this code is found in reference.¹¹

S1. It shows a homogeneous distribution of sulfur and mercury (figure not shown).

S2. Figure 1 gives the elemental distributions of Cl, Hg, S, Na, Al, Si, and K. The chlorine distribution clearly follows the patchy stripes. There is no observable correlation between Cl and Na (within our detection limits). More precisely, hollow light gray areas contain more Cl and less Hg and S than in undamaged cinnabar. Cl is also concentrated in lilac-gray zones, and in some bulging black spots, but not in the bottom thin black line. Therefore, distinct types of black deposits are likely present on S2 with different compositions. Various blackening processes are thus expected. A good correlation exists between Al, Si, and K. The later show higher concentrations in rust spots.

(11) Sole, V. A.; Papillon, E. PyMCA: X-ray Spectra Visualization and Analysis in Python. NOBUGS 2004. (Available at <http://www.esrf.fr/computing/bliss/downloads>).

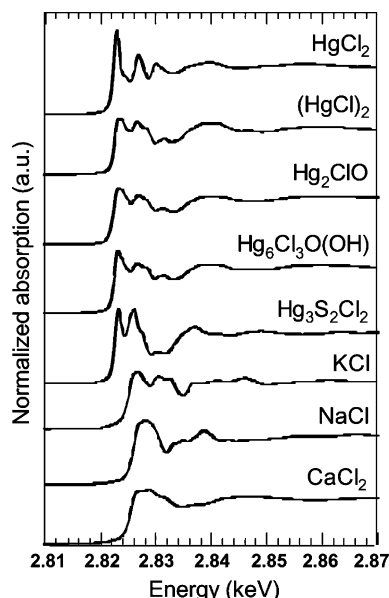


Figure 4. Chlorine K-edge XANES spectra of chlorinated references: CaCl_2 , NaCl , KCl , corderoite ($\text{Hg}_3\text{S}_2\text{Cl}_2$), egglestonite ($\text{Hg}_6\text{Cl}_3\text{O}(\text{OH})$), terlinguaite (Hg_2ClO), calomel (HgCl_2), and HgCl_2 .

S3. As shown in Figure 2, sulfur is particularly concentrated in both black and brown areas. In these parts, mercury is depleted whereas it is concentrated in the red powdery parts. Cl and Na distributions are correlated, outlining spots of NaCl . They are present in both red and black areas. Here again, high amounts of Al, Si, and K correspond to white/orange superficial protrusions.

According to the above results, the correlations between atomic compositions and alterations lead to the hypothesis that, despite similar macroscopic aspects, the alteration processes are different in S2 and S3. In particular, these results indicate that chlorine and sulfur are primarily involved in the chemical degradation of S2 and S3, respectively. Therefore, micro X-ray absorption spectroscopy at both Cl and S K-edges was required to reveal their speciation in the different degraded domains, and their possible role in the degradation reactions.

(b) Micro X-ray Absorption Spectroscopy Analyses. Principle and Reference Spectra. The principle of the XANES is to probe the local chemical speciation of elements by measuring the X-ray absorption coefficient versus the energy of the excitation beam. This method is sensitive to local chemical environment, i.e., oxidation state, geometry, and surrounding atoms. A good review of various chlorinated species can be found in ref 12. Reference spectra of relevant chlorinated species (corderoite ($\text{Hg}_3\text{S}_2\text{Cl}_2$), egglestonite ($\text{Hg}_6\text{Cl}_3\text{O}(\text{OH})$), terlinguaite (Hg_2ClO), calomel (HgCl_2), HgCl_2 , CaCl_2 , NaCl , KCl) were measured and are given in Figure 4. The most striking difference between mercury versus alkali and alkaline earth chlorides is the 5-eV low-energy shift of the absorption edge.

Sulfur-XANES spectra exhibit higher variety, reflecting the sulfur oxidation-state diversity. Two sets of reference compounds were measured. Figure 5 shows sulfide (HgS (cinnabar and metacinnabar), As_2S_3 , Sb_2S_3 , yellow and red Cd_2S_3 , $\text{Hg}_3\text{S}_2\text{Cl}_2$) and native sulfur (S_8).

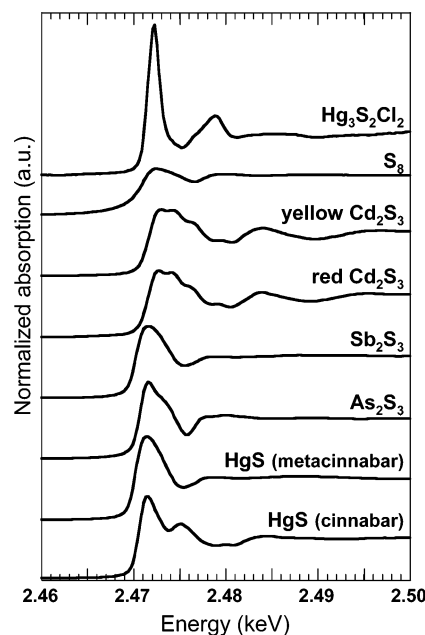


Figure 5. Sulfur K-edge XANES spectra of reduced sulfur references: cinnabar (HgS), metacinnabar (HgS), As_2S_3 , Sb_2S_3 , red Cd_2S_3 , yellow Cd_2S_3 , native sulfur (S_8), and corderoite ($\text{Hg}_3\text{S}_2\text{Cl}_2$).

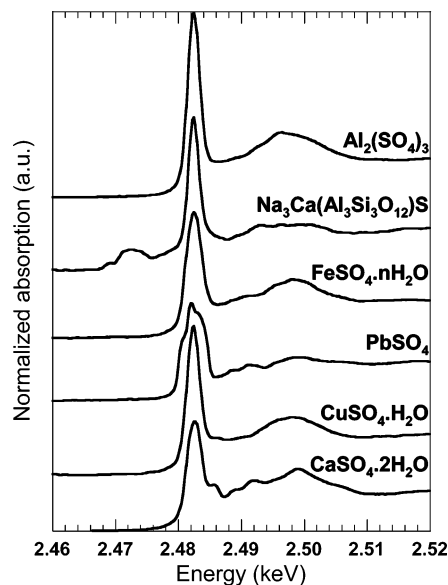


Figure 6. Sulfur K-edge XANES spectra of sulfate references: gypsum ($\text{CaSO}_4 \cdot 2\text{H}_2\text{O}$), $\text{CuSO}_4 \cdot \text{H}_2\text{O}$, PbSO_4 , $\text{FeSO}_4 \cdot n\text{H}_2\text{O}$, lapis lazuli ($\text{Na}_3\text{Ca}(\text{Al}_3\text{Si}_3\text{O}_{12})\text{S}$), and $\text{Al}_2(\text{SO}_4)_3$.

nations α' - HgS and β - HgS are found in the literature),^{13–15} reference spectra of both minerals were specifically compared. The two phases can clearly be differentiated using XANES: cinnabar exhibits a doublet at 2.4718 and 2.4747 keV whereas metacinnabar shows a single peak at 2.4718 keV.

Spectra of various sulfate compounds (Ca, Cu, Pb, Fe, Al) are shown in Figure 6. Most of the spectra feature an intense white line whose energy ranges from 2.471 keV for S^{+II} to ~ 2.482 keV for S^{+VI} . Lapis lazuli, which is a mixture of sulfide and sulfate, is added in Figure 6.

(13) Wang, H.; Zhu, J.-J. *Ultrason. Sonochem.* **2004**, *11*, 293–300.

(14) San Miguel, A.; Polian, A.; Itie, J. P. *J. Phys. Chem. Solids* **1995**, *56* (3–4), 555–558.

(15) Fellner, P.; Khandl, V. *Chem. Pap.* **1999**, *53* (4), 238–241.

(12) Huggins, H. E.; Huffman, G. P. *Fuel* **1995**, *74* (4), 556–569.

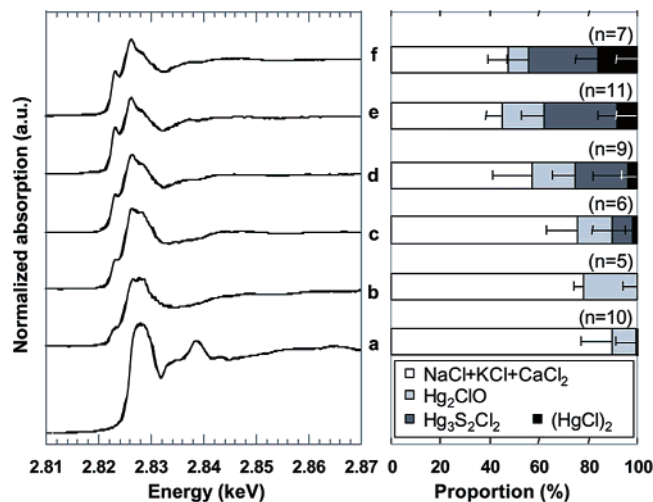


Figure 7. Chlorine K-edge XANES spectra: Cl hot spot on S3 (a), red on S2 (b), rust on S2 (c), light gray on S2 (d), lilac-gray on S2 (e), and bulging black spots (f). Histograms: averaged composition as derived from the linear combination of reference spectra. The bars indicate the standard deviation for n fitted spectra in a given region (see text for details).

Cl K-Edge. Figure 7 shows μ -XANES spectra at the Cl K-edge, acquired at different spots of S2 and S3. Results were compared to references (Figure 4). Spectra obtained on Cl-rich regions on S3 confirm the main presence of NaCl (Figure 7a). On the contrary, spectra obtained on S2 are different and feature additional peaks at 2.823 and 2.826 keV that may indicate the presence of chlorine bonded to mercury (Figure 7b–f). The XANES spectra were normalized and fitted as linear combination of the reference spectra of pure NaCl, KCl, CaCl_2 , HgCl_2 , and $(\text{HgCl})_2$, $\text{Hg}_3\text{S}_2\text{Cl}_2$, $\text{Hg}_6\text{Cl}_3\text{O}(\text{OH})$, and Hg_2ClO . The proportions of the different components in each altered zone are plotted in Figure 7 (average on a minimum of 5 points per zone). The amount of HgCl_2 and eglestonite ($\text{Hg}_6\text{Cl}_3\text{O}(\text{OH})$) was always zero and hence is not indicated in the histograms. Both spectra and fits show that the relative proportion of mercury compounds increases with a darker aspect of the sample on S2 (from Figure 7b to f). In red and rust parts (Figure 7b, c), less than $\sim 20\%$ of the chlorine is coordinated with mercury whereas the set of mercury species (corderoite, terlinguaite, and calomel) represents $\sim 40\text{--}50\%$ of the chlorine environment in gray bands and black spots of S2 (Figure 7d–f). Besides, the proportion of chloride-mercury bonds is more important in the lilac-gray flat parts (Figure 7e) than in hollowly light pink parts (Figure 7d). This agrees with the lower amount of Hg in these lighter parts.

S K-Edge. μ -XANES at the sulfur K-edge was performed on different points of S1, S2, and S3. Spectra obtained on S1 are mainly characteristic of red cinnabar (Figure 8a). In all degraded regions of S2 and S3, XANES spectra indicate an additional contribution from sulfate compounds (Figure 8b–g). The detailed analysis of the spectrum features, from 2.487 to 2.51 keV, and particularly the secondary maximum at 2.493 keV pinpoints the presence of calcium sulfate, namely, gypsum (see reference spectrum, Figure 6). Each spectrum was normalized and fitted as a linear combination of spectra of pure cinnabar (HgS), metacinnabar (HgS), sulfur (S), corderoite ($\text{Hg}_3\text{S}_2\text{Cl}_2$), and gypsum ($\text{CaSO}_4 \cdot 2\text{H}_2\text{O}$). An example of fit is given in Figure 9. The

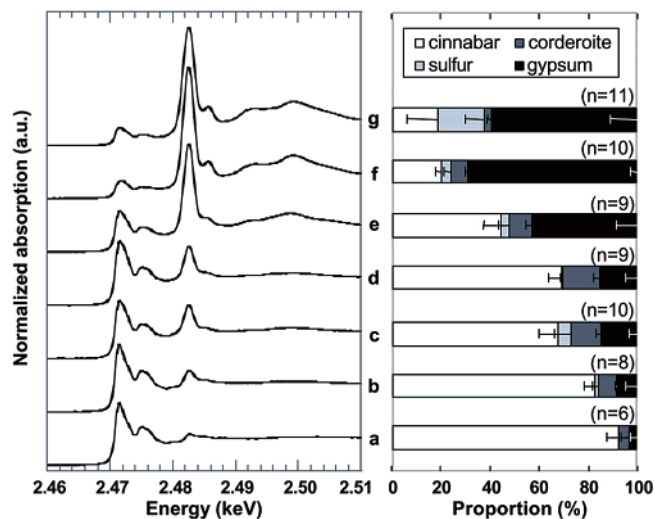


Figure 8. Sulfur K-edge XANES spectra: red S1 (a), light red on S3 (b), hollow light pinky gray on S2 (c), lilac-gray on S2 (d), brown on S3 (e), black on S3 (f), and rust on S3 (g). Histograms: averaged composition as derived from the linear combination of reference spectra. The bars indicate the standard deviation for n fitted spectra in a given region (see text for details).

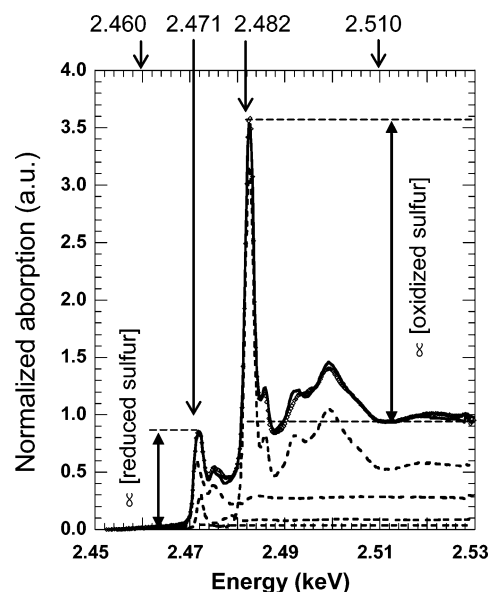


Figure 9. Computation on the μ -XANES spectra at the S K-edge: fit of the experimental data (plain) by combination of cinnabar, sulfur, corderoite, and gypsum spectra (dotted) and estimation of the reduced and oxidized sulfur concentrations by measuring the fluorescence intensity at four specific energies.

contribution of metacinnabar was always found to be zero. The coefficients of the different species were calculated for each spectrum, and the average and standard deviation obtained on at least 6 points for each degradation type are plotted in Figure 8. In the red parts of S1 (Figure 8a), reduced sulfur represents more than $98 \pm 2\%$ of sulfur speciation. In the light red parts of S3 (Figure 8b), the proportion of sulfated species slightly increases ($8 \pm 4\%$). Light gray (Figure 8c) and lilac parts (Figure 8d) of S2 are comparable in terms of sulfur environment with $\sim 15\%$ sulfur as corderoite and as sulfate. The amount of sulfate dramatically increases in the dark parts of S3 reaching values of $43 \pm 8\%$ in brown zones (Figure 8e) and up to $69 \pm 2\%$ in black regions (Figure 8f). These figures show a positive correlation between

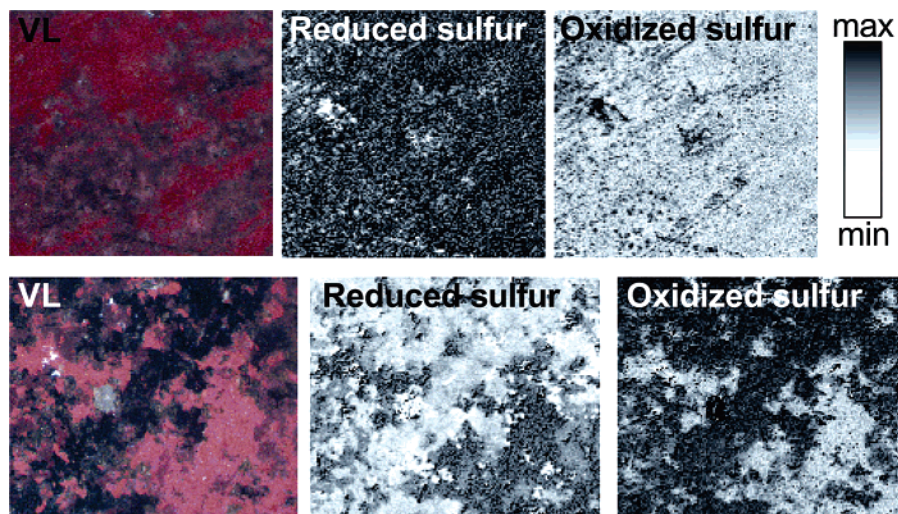


Figure 10. Normalized images of the distribution of the reduced and oxidized sulfurs on S2 (top, $7 \times 7 \text{ mm}^2$) and S3 (bottom, $8 \times 7 \text{ mm}^2$). Pixel size, $50 \times 50 \mu\text{m}^2$; dwell time, 1.1 s.

blackening process maturation and the sulfate/sulfide ratio. In particular, it strengthens our previous hypothesis (see section on visible light microscopy) that, in S3, brown to black shades reflect mainly a gradient in sulfate concentration. Furthermore, metacinnabar is never detected, in particular in black regions where its presence could have been expected, conferring the literature.^{3–5} High sulfate concentrations are observed the white/orange particles, in both S2 and S3 (Figure 8g).

To map the distribution of oxidized and reduced states of sulfur over S2 and S3 areas, a simpler quantification method was used. It relies on the fact that reduced sulfurs (native sulfur, cinnabar, metacinnabar, corderoite) and oxidized sulfur spectra exhibit well-resolved characteristics peaks at 2.471 and 2.482 keV, respectively. It is possible to estimate the relative concentration of reduced and oxidized sulfurs by measuring the X-ray fluorescence intensity at four exciting energies: (1) at 2.471 keV, to favor the excitation of the reduced sulfurs; (2) at 2.482 keV, to favor the excitation of the oxidized sulfurs; (3) at 2.460 keV, to measure selectively the contribution of mercury; (4) at 2.510 keV, to measure the global fluorescence of sulfur, whatever its speciation.

The fluorescence intensity at the two former energies is used for the normalization. The relative concentration of reduced and oxidized sulfurs are given by

$$[\text{reduced sulfur}] \propto \frac{I(2.471) - I(2.460)}{I(2.510) - I(2.460)} \text{ and}$$

$$[\text{oxidized sulfur}] \propto \frac{I(2.482) - I(2.510)}{I(2.510) - I(2.460)} \quad (1)$$

where $I(x)$ is the fluorescence intensity at the energy x (in keV) (see Figure 9).

This approach was applied to each pixel of the four images recorded by μ -XRF at the four specific energies and used to derive the distribution maps of sulfide and sulfate on S2 and S3 (Figure 10).

S2. Sulfates are concentrated in the rust spots, in the thin bottom black line, and in other parts that do not correspond to any distinguishable area, with light microscopy. They follow

particular orientation, mainly on the top left part of the map. Generally, the sulfation is lower on S2 than on S3.

S3. The oxidized sulfurs map matches with blackened regions whereas the reduced sulfurs map is in good correlation with mercury location and is more intense in red areas. Brown zones are a mixture of sulfides and sulfates. Besides, relatively high concentrations of sulfate are observed in the Al–Si–K-rich orange protrusions.

(c) Transversal Cross Sections. Analyses on transversal cross sections were conducted in order to image the in-depth distribution of painting and degradation products. The light microscopy picture of the cross section lets appear a white underlying mortar under a $\sim 40\text{-}\mu\text{m}$ -thick red layer, covered with a thin black layer. On the left part of the map, a $\sim 20\text{-}\mu\text{m}$ -diameter black grain can be seen (Figure 11, VL).

The μ -XRF analysis was performed at 4.1 keV, which enables the excitation of calcium. The use of a Fresnel zone plate enables to reduce the beam size to $0.4 \times 0.5 \mu\text{m}^2$. A microprobe is essential to resolve the small structures. Atomic mappings of Ca, Al, Si, K, Na, Cl, Hg, and S are shown in Figure 11. Ca is not only present in the white underlying mortar but is also heterogeneously mixed with cinnabar in the red layer, with a greater concentration in the black left grain. The superficial black layer contains a relatively high amount of calcium. Al, Si, and K distributions are similar, with a hot spot on the surface. Cl is more concentrated in the black superficial layer and shows a diffusion-like distribution around the Ca particles. In the red layer, Hg and S are obviously co-localized (cinnabar) and are surrounded by calcium. The ratio S/Hg is slightly greater on the black superficial layer. Finally, Na has a homogeneous distribution in the cinnabar.

Following the previously used protocol, four images at four characteristic energies were recorded and the sulfate and sulfite maps have been derived (Figure 11). The maps of oxidized and reduced sulfurs show two distinct distributions: sulfates are localized within a thin superficial film of $\sim 4 \mu\text{m}$ onto a thick red layer of cinnabar (cinnabar distribution is derived from the good correlation between the reduced sulfurs and mercury maps).

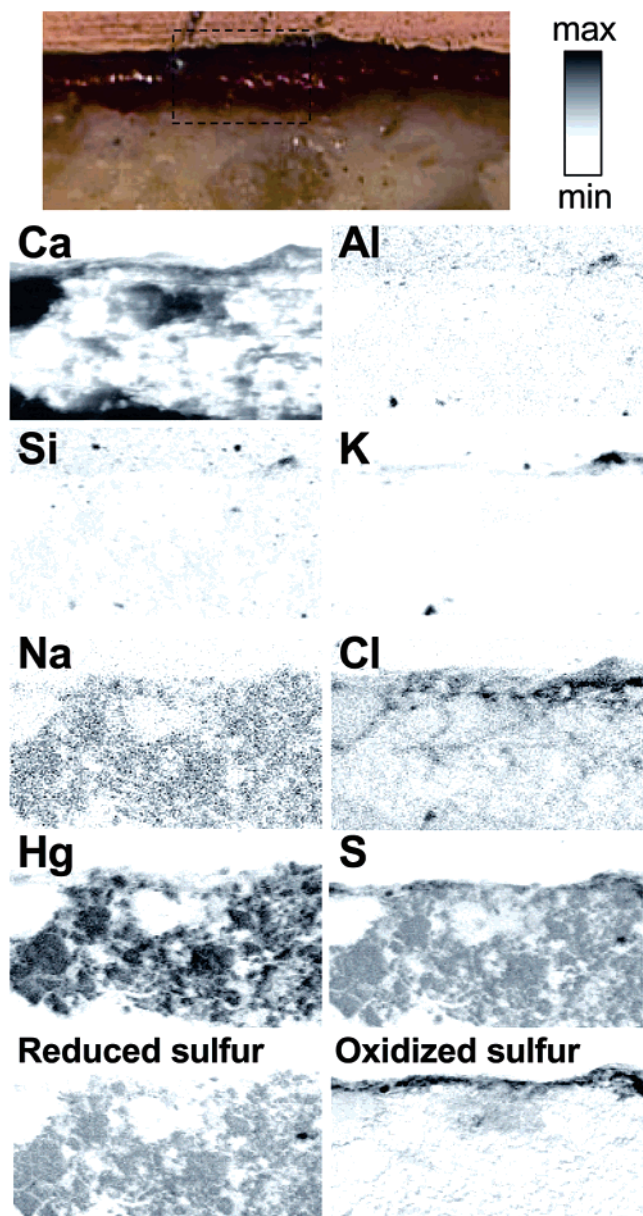


Figure 11. VL of a transversal cross section. The dotted rectangle indicates the area analyzed by μ -XRF: atomic distribution of Ca, Al, Si, K, Na, Cl, Hg, and S (obtained with an exciting beam of 4.1 keV); images of reduced and oxidized sulfurs (see text for details). Pixel size, $0.5 \times 0.5 \mu\text{m}^2$; map size, $60 \times 95 \mu\text{m}^2$; dwell time, 0.3 s.

DISCUSSION

Even if, at first sight, S2 and S3 seem rather similar, visible light and X-ray microscopies indicate clear differences in both aspect and chemical compositions of the degraded regions.

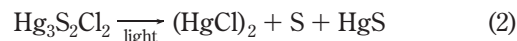
Mechanism Involving Chlorine. In S2, the peculiar distribution of chlorine in debased regions indicates its possible role in the degradation process. The presence of various chlorine–mercury compounds is confirmed by μ -XANES at the Cl K-edge. As discussed above, the spectroscopic analysis indicates that the degradation products are a complex mixture, with the possible combination of terlinguaite (Hg_2ClO), corderoite ($\text{Hg}_3\text{S}_2\text{Cl}_2$), and calomel (HgCl_2). The presence of corderoite is further supported by similar analyses at the sulfur K-edge (XANES spectra are indeed better fitted by introducing corderoite in the linear combination).

According to the literature, chlorine can act in two ways in the blackening process: (1) catalysis of the photochemical reaction,⁹ $\text{HgS} \rightarrow \text{Hg} + \text{S}$; (2) reaction with Hg or with HgS leading to various Hg–Cl compounds.^{6–9}

Mc Cormack observed that nonphotosensitive cinnabar becomes superficially photosensitive after exposure to halogens: “crystals of cinnabar were exposed to brine saturated of KCl and KI, kept in the dark and shaken occasionally, for 2 yr. The washed and dried, still bright red cinnabar turned black on exposure to sunlight within 1 h. Grinding, however, restored the original bright color, and no darkening of the material was observed thereafter on exposure to sunlight, even after days”.⁶ In an other experiment, he noted that “cinnabar in contact with a slightly saline (NaCl) solution blackens while the solution is evaporated under sunlight”.⁷ In our case, an external contamination of chlorine is suspected due to the identification of spots of NaCl. The presence of NaCl could have various origins (sea neighboring, use of materials such as *cera punica*, which was often applied on paintings as protection and shiny overlayer. This type of wax was commonly prepared with seawater as explained by Plinius. (“Punica fit hoc modo: ventilatur sub diu saepius cera fulva, dein fervet in aqua marina, ex alto petita, addito nitro. Inde lingulis hauriunt florem, id est candidissima quaeque, transfunduntque in vas, quod exiguum frigidae habeat, et rursus marina decocunt separatim; dein vas ipsum aut aquam refrigerant.” Plinius, *Naturalis Historia*—XXI, [49].

“*Punica wax is made this way: yellow beeswax is often exposed to air for a long time, then it is boiled in water from high sea, to which is added nitre. Then, wax bloom is removed with a spoon, e.g. the whitest part, and is poured into a pot containing a bit of cold water; this part is boiled again in seawater; and then the vas is cold.*” Plinius, *Naturalis Historia*—XXI, [49].)

The presence of chlorine in degraded vermilion has already been observed in paintings. Calomel ($(\text{HgCl})_2$) was identified by Raman spectroscopy in the white particles present in the gray crust on the surface of Benozzo Gozzoli’s *Virgin and Child Enthroned* and the *Saint John on Patmos* attributed to the Workshop of the Master of the Female Half-lengths. Spring et al. proposed a mechanism for the photoinduced formation of calomel from corderoite ($\text{Hg}_3\text{S}_2\text{Cl}_2$):³



This hypothesis is supported by the identification of calomel, by X-ray diffraction, in the gray photodegradation product of corderoite.⁸

Keune and Boon studied the composition of darkened vermilion in Rubens’s *Portrait of a Lady* and Christian van Couwenberg’s *Minerva and Hercules Opening the Doors for Victory*, by secondary ion mass spectrometry. They observed in degraded layer cluster ions similar to that obtained when analyzing a mixture of HgS and HgCl_2 . The presence of calomel ($(\text{HgCl})_2$) could not be proven by SIMS,⁹ neither is it clearly established by the present approach: in Figure 4, no clear differences are perceptible between the Cl K-edge XANES spectra collected from $(\text{HgCl})_2$ (calomel), Hg_2ClO (terlinguaite), and $\text{Hg}_6\text{Cl}_3\text{O}(\text{OH})$ (eglestonite), all contain-

ing Hg–Hg bonds.¹⁶ (HgCl)₂ decomposes by disproportionation under the action of light at room temperature:



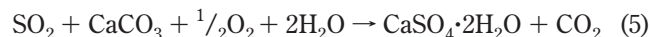
The presence of the mercuric(II) compound, HgCl₂, in our case, was not clearly shown, but it cannot be completely excluded. The environmental conditions of Pompeian mural paintings differ from those of oil or tempera paintings conserved in museums. The former are stored in a rather stable atmosphere, and only the volatile molecules are susceptible to escape from the paintings. On the contrary, the latter Pompeian walls are exposed to sun and moisture, and therefore, the washing action of water must be taken into account. In this context, the fact that HgCl₂ is soluble in water may explain why it is not observed here whereas it was identified in oil paintings.⁹ Conversely, (HgCl)₂ being slightly soluble, is less sensible to weathering processes.

Basic considerations of colors support our model: Hg and Hg₂ClO are black whereas (HgCl)₂ is white, which may explain the pink-gray shades. Corderoite has a lilac aspect very similar to some colors observed on the altered region of S2.

Mechanism Involving Sulfation. The black thin line on the bottom of S2 and debased regions in S3 share similar chemical composition and suggest a similar degradation process: calcite sulfation. This reaction of SO₂ on CaCO₃ could be analogous to the one observed on carbonate-based stones submitted to sulfured pollution (formation of “black crusts”). Here, SO₂ can come from polluted atmosphere but can also be formed by oxidation of sulfur (produced by decomposition of HgS (1) and possibly identified by XANES at the sulfur K-edge (Figure 8)):



This reaction would explain why sulfation is favored on cinnabar and does not spread on other pigments. The total chemical reaction of SO₂ with calcite can be described by the following scheme:



The above reaction can follow different pathways. Depending on the conditions, the oxidation step is thought to occur either before^{15,17} or after^{18–20} the reaction of SO₂ with CaCO₃.

The presence of gypsum in ancient painting does not necessarily indicate an altering sulfation process. Gypsum was sometimes added as a white pigment in the lime plaster.^{21–22} Mortar from *Thermae Stabiane* and *House of Fabius Rufus* in Pompeii

shows abundant gypsum mixed with calcite and a small amount of quartz.²³ The authors explain that it indicates the use of a lime-gypsum mortar for the final layer, which would be compatible with the *tempera* technique. In our case, gypsum is absent in the intact painting. Moreover, the transversal analyses clearly show that sulfates are present only in a superficial layer of ~5 μm, which strongly suggests that gypsum does result from a reaction of the painting surface with the environment. CaCO₃ is present not only in the mortar but it also mixed with cinnabar in the colored layer, so provides an available source of calcium on the surface.

The relationship between sulfate and the presence of Al, Si, and K is not that simple. It is noteworthy that the distribution of Al, Si, and K, mainly on the surface of the painting (Figure 10), is in favor of an external contamination. This hypothesis agrees with results obtained by Sabbioni and Maravelaki-Kalaitzaki.^{24,25} They studied the origin of various elements detected in black crusts on historical marble and limestone monuments by comparison of the atomic composition of black crust, stone, and soil dust. It was shown that the major source of Si, Al, K, Na, and Mg was soil dust. Some correlations between the distribution of sulfates and Al, Si, and K, in both S2 and S3, can be observed. In this context, research on the use of calcite in sulfur oxide removal from flue gas demonstrated that potassium ions promote the sulfation.^{18,19} Bernal and Bello gave a short review of research on the catalytic effect of different airborne particles on the reaction of SO₂ on CaCO₃. Although the role of Al, Si, and K is not mentioned, this paper reports that fly ashes favor the formation of gypsum.²⁰ Therefore, it seems realistic that Al, Si, and K as well as fly ashes present in dark black areas of S3 act as catalysts of sulfation reaction.

The fact that degradation remains a superficial phenomenon can be explained by the promoting action of two external agents on reaction 1: light^{6,26,27} and chlorine.^{6,9} Besides, sulfation requires a supply of SO₂, which can come from polluted environment or from the oxidation of S, formed, in surface, by (1).

One controversial point deals with the origin of the colors, since gypsum is white or light in normal conditions. Black coating could be imputed to the additional presence of airborne organic pollutants, carbonaceous particles, dust, trapped inside gypsum crystals, similarly to what happens in black crusts.¹⁷ Conversely, gypsum distribution is not restricted to black areas. The rust areas could be the combination of brown or orange soil dust and white gypsum. In addition, gypsum is also detected in red areas (top-left corner of S2). It may be present as a thin transparent layer over the cinnabar. So, curators and restorers must beware of the possible invisible presence of gypsum: the absence of black crust does not systematically mean an absence of sulfation.

Nevertheless, we point out that comparative analyses on thin sections (polarized light microscopy) obtained from samples coming from black crusts on different types of outdoor monuments and black coating on a red cinnabar layer from roman wall paintings reveal remarkable petrographic differences (structure,

(16) Brodersen, K.; Göbel, G.; Liehr, G. *ZAAC* **1989**, 575, 145–153.

(17) Nuhoglu, Y.; Oguz, E.; Uslu, H.; Ozbek, A.; Ipekoglu, B.; Ocak, I.; Hasenekoglu, I. *Sci. Total Environ.* **2006**, 364 (1–3), 272–283.

(18) Anderson, D. C.; Anderson, P.; Galwey, A. K. *Fuel* **1995**, 74 (7), 1018–1023.

(19) Anderson, D. C.; Anderson, P.; Galwey, A. K. *Fuel* **1995**, 74 (7), 1024–1030.

(20) Bernal, J. L. P.; Bello, M. A. *Ind. Eng. Chem. Res.* **2003**, 42, 1028–1034.

(21) Perez-Alonso, M.; Castro, K.; Alvarez, M.; Madariaga, J. M. *Anal. Chim. Acta* **2004**, 524, 379–389.

(22) Bersani, D.; Antoniolli, G.; Lottici, P. P.; Casoli, A. *Spectrochim. Acta, Part A* **2003**, 59, 2409–2417.

(23) Zanella, E.; Gurioli, L.; Chiari, G.; Ciarallo, A.; Cioni, R.; De Carolis, E.; Lanza, R. *Phys. Earth Planet. Inter.* **2000**, 118, 227–240.

(24) Sabbioni, C. *Sci. Total Environ.* **1995**, 167, 49–55.

(25) Maravelaki-Kalaitzaki, P. *Anal. Chim. Acta* **2005**, 532, 187–198.

(26) Gustin, M. S.; Biester, H.; Kim, C. K. *Atmos. Environ.* **2002**, 36, 3241–3254.

(27) Pal, B.; Ikeda, S.; Ohtani, B. *Inorg. Chem.* **2003**, 42, 1518–1524.

texture, composition), which are also confirmed by in situ observations.²⁸ Additional analyses are being carried out to better identify the composition of this black coating and to explain its color.

CONCLUSIONS

The degradation of cinnabar paintings is known as a complex phenomenon. In the present work carried out on three samples representative of various alteration states, at least two different mechanisms have been identified, and two possible distinct chemical pathways are proposed. On one hand, the reaction of chlorine with cinnabar leads to the formation of gray chlorine–mercury compounds. On the other hand, the sulfation of calcite results in the development of black coatings on the painting surface. These two pathways are likely not independent since the decomposition of cinnabar into Hg and S, catalyzed by Cl, could promote concomitantly (i) the reaction of Hg with Cl and (ii) the formation of SO₂ and its forthcoming deposition on calcite. This assumption is also supported by our observations on the systematic coexistence between sulfates, native sulfur, and corderoite. However, other sulfation mechanisms can be envisaged, most

likely atmospheric contamination (SO₂) or bacterial activities. Such information is essential for curators and restorers to adapt further treatments and to improve the storage conditions. The analyses benefited from the high chemical sensitivity, low detection limit, and high lateral resolution of synchrotron-based X-ray microspectroscopy. Wider selection of samples, representative of different environments, would be required to assess a more accurate correlation. A systematic correlation scheme between atomic composition measurements by microanalytical techniques and macroscopic alteration signs observed by visible light microscopy can be envisaged.

ACKNOWLEDGMENT

This study was funded by grants from ESRF (experiment ME-1092). We thank P.-J. Chiappero (Museum National d'Histoire Naturelle, Paris, France), R. Garcia-Moreno, E. Welcomme, and P. Walter (Centre de Recherche et de Restauration des Musées de France, Paris, France) for providing us with reference compounds.

Received for review July 6, 2006. Accepted August 22, 2006.

AC0612224

(28) Gratziu, C., unpublished data.